

# Weakly faceted cellular patterns *versus* growth-induced plastic deformation in thin-sample directional solidification of monoclinic biphenyl

Tamás Börzsönyi,<sup>1,2,\*</sup> Silvere Akamatsu,<sup>1</sup> and Gabriel Faivre<sup>1</sup>

<sup>1</sup> *INSP, UPMC Univ. Paris 6, CNRS UMR 7588, 140 rue de Lourmel, 75015 Paris, France*

<sup>2</sup> *Research Institute for Solid State Physics and Optics, POB 49, H-1525 Budapest, Hungary*

(Dated: March 10, 2022)

We present an experimental study of thin-sample directional solidification (T-DS) in impure biphenyl. The plate-like growth shape of the monoclinic biphenyl crystals includes two low-mobility (001) facets and four high-mobility {110} facets. Upon T-DS, biphenyl plates oriented with (001) facets parallel to the sample plane can exhibit either a strong growth-induced plastic deformation (GID), or deformation-free weakly faceted (WF) growth patterns. We determine the respective conditions of appearance of these phenomena. GID is shown to be a long-range thermal-stress effect, which disappears when the growth front has a cellular structure. An early triggering of the cellular instability allowed us to avoid GID and study the dynamics of WF patterns as a function of the orientation of the crystal.

PACS numbers: 64.70.M-, 81.10.Aj, 64.70.D-, 68.70.+w

## I. INTRODUCTION

Directional solidification of dilute alloys gives rise to complex out-of-equilibrium growth patterns. The control of these patterns is a central issue in materials science [1] and raises fundamental problems in nonlinear physics. The basic phenomenon in the field is the bifurcation from a planar to a digitate growth front, which occurs when the solidification rate  $V$  exceeds a critical value  $V_c \approx GD/\Delta T_o$ , where  $G$  is the applied thermal gradient,  $D$  is the solute diffusion coefficient in the liquid and  $\Delta T_o$  is the thermal gap of the alloy [2, 3]. The morphology of the fingers above the critical point evolves from rounded cells at  $(V - V_c)/V_c \ll 1$  to dendrites (parabolic tip and sidebranches) at  $(V - V_c)/V_c \gg 1$  [4]. The dominant factors in the process are the diffusion of the chemical species in the liquid, and the resistance of the solid-liquid interface to deformation, which is determined by  $G$  and the physical properties of the interface itself, namely, its surface tension  $\gamma$  and kinetic coefficient  $\beta = \partial(\delta T_k)/\partial V$ , where  $\delta T_k$  is the kinetic undercooling. While the value of  $V_c$  is approximately independent of  $\gamma$  and  $\beta$ , the characteristics of the cellular or dendritic patterns at  $V > V_c$  crucially depend on these properties, especially, on their anisotropy [5, 6, 7, 8, 9, 10]. A fundamental distinction must be made between nonfaceted and faceted alloys, the latter being the alloys, in which  $\gamma(\mathbf{n})$  and/or  $\beta(\mathbf{n})$  have cusp singularities for some orientations of  $\mathbf{n}$ , where  $\mathbf{n}$  is the normal to the interface referred to the crystalline axes. The distinction between two-dimensional (or thin) and three-dimensional (or bulk) solidification is also important.

This article reports the results of an experimental investigation of pattern formation during thin directional

solidification (T-DS) in a substance forming faceted (monoclinic) crystals, namely, impure biphenyl. The geometry of the experiments is specified in Figure 1. We focus on the growth patterns, called weakly faceted (WF) patterns, that bring into play only high-mobility facets. Under usual experimental conditions (*i.e.* far from any roughening transition), facet mobility is controlled by the motion of one-molecule-thick growth steps emitted from certain sites (intersections with crystal dislocations, contacts with other crystals) [11]. A given facet can have a high, or a low mobility depending on whether, or not, it contains such step sources. The high-to-low-mobility transitions of a facet during growth, if any, are due to step sources entering or leaving the facet, and are quite sharp, and thus easily identified on a macroscopic scale [12].

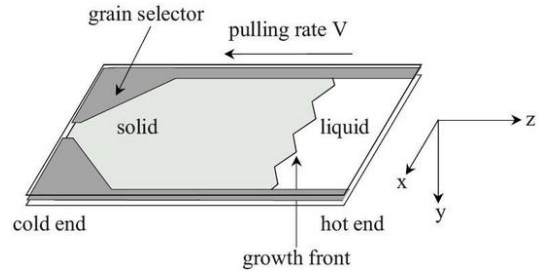


FIG. 1: Geometry of thin directional-solidification (T-DS) experiments. A  $12 \mu\text{m}$ -thick layer of liquid enclosed by glass plates and polymer spacers is pulled toward the cold end in an imposed thermal gradient. The growth front is observed in real time with a polarizing optical microscope.  $z$ : thermal-gradient and growth axis.  $y$ : normal to sample plane and direction of observation.  $x$ : overall direction of the growth front.

Interest in the theory of thin weakly faceted (WF) growth was aroused by experiments by Maurer *et al.* showing that the facet length of free-growth dendrites of  $\text{NH}_4\text{Br}$  followed the same  $V^{-1/2}$  scaling law, where

\*Electronic address: btamas@szfki.hu

$V$  is the dendrite tip growth rate, as the tip radius of nonfaceted dendrites [13]. Ben Amar and Pomeau explained this finding by establishing analytically that the whole morphology of steady free-growth dendrites obeys a  $V^{-1/2}$  scaling law [14] using a purely capillary ( $\beta = 0$ ) 2D model of weak faceting at low undercooling  $\Delta T$  of the liquid. These authors then showed that introducing standard facet kinetics ( $\delta T_k \propto V^n$ , where  $n \leq 2$ ) in the model should not alter these conclusions. Adda Bedia and Hakim [15, 16] gave approximate analytical solutions for free-growth dendrites with capillary facets. Recently, Debierre and coworkers revisited this problem using phase-field numerical simulations [17, 18], and extended the validity of the  $V^{-1/2}$  scaling law to arbitrary  $\Delta T$  and capillary-anisotropy coefficients. Concerning directional solidification, the main theoretical contributions so far are two analytical studies, one dealing with the cellular transition in the particular case when a high-mobility facet is perpendicular to the growth direction by Bowley *et al.* [19] and Caroli *et al.* [20], and the other dealing with steady WF patterns at  $V > V_c$  in crystals with two facets at  $\pm 45^\circ$  from the growth axis by Adda Bedia and Ben Amar [21]. Among the numerous problems left unsolved today, most authors singled out the question of the respective roles of capillary and kinetic anisotropies in WF growth. To tackle this problem is a current challenge for phase-field numerical simulations [17, 22, 23].

With regard to experimental investigations capable of casting light on the dynamics of thin WF patterns, we are aware of studies dealing with mesophase systems [24, 25, 26], but none of dealing with "solid" crystals. A reason for this is the frequent occurrence of large-amplitude plastic deformations –called growth-induced deformation (GID) thereafter– breaking up faceted solid crystals into a multitude of small grains during T-DS. The origin of GID, and the methods of keeping it from happening, if any, are still unclear. Fabietti and Trivedi [27] studied GID during T-DS in impure naphthalene, which has the same crystallographic structure as biphenyl, but their observations were inconclusive as regards the possible existence of deformation-free thin cellular patterns. In this article, we report that GID did not occur during thin free growth (T-FG) of biphenyl crystals indicating that GID basically is a thermal-stress effect generated by the externally applied thermal gradient. Most significantly, we found that GID was also lacking during T-DS when the (deformation-free) growth front was cellular. By triggering the cellular instability at an early stage of T-DS, it was thus possible to grow deformation-free steady WF patterns in impure biphenyl. We present a detailed study of the spatiotemporal dynamics of GID in T-DS samples with single-crystal seeds. This study reveals that the first stage of GID is a long-range process, which occurs only in large-width crystals, and not in the narrow cells of the cellular patterns. Finally, we report a first investigation of thin WF patterns in deformation-free biphenyl crystals for various orienta-

tions of the crystal with respect to the growth direction.

## II. MATERIALS AND METHODS

Biphenyl ( $C_{12}H_{10}$ ) is a transparent substance, which crystallizes into a biaxial birefringent monoclinic phase at  $T_m \approx 70^\circ\text{C}$ . The point group of the crystal has a twofold axis  $\mathbf{b}$  and a mirror plane normal to  $\mathbf{b}$  that contains the other two lattice translations  $\mathbf{a}$  and  $\mathbf{c}$  (Fig. 2). The crystalline parameters are  $a = 0.81$ ,  $b = 0.56$  and  $c = 0.95$  nm, and the angle between  $\mathbf{a}$  and  $\mathbf{c}$  is  $95.1^\circ$  at room temperature [28, 29]. Biphenyl crystals have a perfect (001) cleavage, and various glide systems involving dislocations with Burgers vectors [100] and [010], but not [001] [30]. We show below that, during melt growth, biphenyl exhibits only {001} ("basal"), and {110} facets. (It does not exhibit {100} facets, contrary to naphthalene). The [100] apex angle of the basal facet, *i.e.* the angle between [110] and  $\bar{1}\bar{1}0$ , calculated from the above data is  $69.5^\circ$ . The terminology for the orientation of the crystals employed hereafter is as follows. Crystals with (001) parallel to the sample plane are called (001)-oriented crystals. Their in-plane orientation is either specified by the angle  $\theta_a$  of  $\mathbf{a}$  and the growth axis (called  $z$ , see Fig. 1), or designated as (001)[100]- or (001)[010]-orientation when  $\theta_a = 0^\circ$  or  $\theta_a = 90^\circ$ , respectively. Crystals deviating from the (001)-orientation are called "tilted", and the angle of their basal plane and the sample plane is denoted  $\omega$ . Crystals with their basal plane nearly perpendicular to the sample plane are called "edge-on".

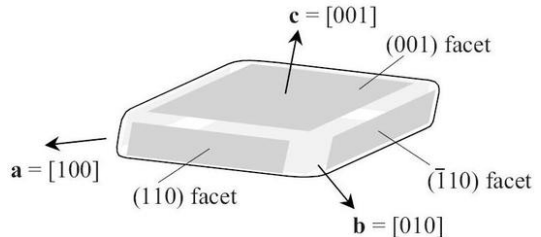


FIG. 2: Melt growth shape of a biphenyl crystal (schematic).

The observations were performed in commercial biphenyl (Fluka, 99.9 %) unless otherwise mentioned. A few experiments were made with biphenyl doped with 1 wgt% of camphor. The methods of preparation and observation of the samples are explained elsewhere [9, 31, 32], and need only to be briefly outlined here. The crucibles consist of two parallel glass plates separated by polymer spacers. Their inner dimensions are of 60mm along  $z$ , 8mm (width) along  $x$ , and  $12\mu\text{m}$  (thickness) along  $y$ . A funnel-shaped grain selector is created near the cold end of the crucibles by using spacers of an appropriate shape (Fig. 1). The crucibles are filled with the liquid compound under controlled Argon atmosphere, quenched to room temperature, and sealed. They

are then inserted into a T-FG or a T-DS setup, and observed in side view by videomicroscopy. Polarized light was used in order to take benefit of the birefringence of the crystals.

T-FG was carried out with a commercial hot stage (IN-STECH, HS1-i) mostly for the purpose of preparing single-crystal seeds for T-DS. The temperature distribution in the setup is not perfectly uniform, but has a shallow depression at the center of the window of observation. This feature can be utilized to grow single-crystal seeds. The temperature of a polycrystalline sample is increased until all the grains melt except the one (the future seed) that is located at the minimum of the temperature distribution. The melting is pursued until the seed detaches itself from the glass plates, is carried away by flows existing in the liquid, and redeposited with, generally, its basal facet closely aligned with the sample plane. The temperature is then decreased step by step in order to make this (001)-oriented single crystal grow without (or with as little as possible) morphological instability. It should be noted that, during this process, the crystal is a thin plate limited by two blocked (deprived of step sources) basal facets, which are basically not in contact with the glass walls. Some crystals had a small residual misalignment and collided with a glass wall during growth. Crystals that filled the sample without hitting the glass walls ( $\omega < 0.01^\circ$ ) were selected as seeds for T-DS. These crystals kept a uniform optical contrast during growth indicating that no noticeable GID occurred during T-FG. The fully solidified samples were then slowly cooled to room temperature, and transferred to the T-DS setup. A weakly contrasted rectilinear striation parallel to the direction [010] appeared at  $\Delta T \approx 10\text{K}$  during cooling, and persisted in the non-melted part of the samples after they were inserted into the T-DS setup. However, they were not transmitted to the grown crystal during T-DS indicating that they did not pertain to the bulk of the crystal, but to the layer of matter comprised between the crystal and the glass walls that solidified during cooling to room temperature. The crystallographic orientation of the striae and the presence of microbubbles are suggestive of slip bands left by [010] dislocations gliding in the (100) plane.

T-DS experiments were performed using a home-built stage made of two independent thermally regulated copper blocks separated by a several millimeters-wide gap, in which the solidification front sits. During this study,  $G \approx 5.6 \text{ Kmm}^{-1}$ , unless otherwise mentioned. The translation velocity of the samples is stable to within  $\pm 2\%$  in the explored range ( $0.1\text{-}30 \mu\text{ms}^{-1}$ ). In addition to a standard T-DS stage, we used a new "rotating T-DS stage", to be presented in a future publication, with which it is possible to rotate the sample about  $y$ , that is, to change the in-plane orientation of the crystal during solidification. The microstructure of the non-melted part (seed) of the sample at the beginning of a T-DS run is an all-important experimental factor that can be largely controlled by an appropriate design of the first stages of T-

DS. The main alternative is to include, or not, a low- $V$  growth through the grain selector prior to the T-DS run proper. A few as-quenched samples were solidified without grain selection, and exhibited a strongly faceted mode of growth. As a general rule, as-quenched samples were solidified with grain selection, which led to a complete elimination of all the tilted grains (see Section III B 2).

A cellular instability was observed during T-DS of (001)-oriented grains under conditions, which will be specified later on. We measured  $V_c$  at  $G = 5.6 \text{ Kmm}^{-1}$  in these grains by the method explained in Ref. [31]. Three types of samples must be distinguished: fresh samples of commercial biphenyl, samples of commercial biphenyl having undergone a T-FG or T-DS solidification/melting cycle at low  $V$  (as is the case of samples with single-crystal seeds) designated as "purified" hereafter, and samples of camphor-doped biphenyl. We found  $V_c = 4.5 \pm 1.5 \mu\text{ms}^{-1}$  in fresh undoped samples,  $V_c > 15 \mu\text{ms}^{-1}$  in purified samples, and  $V_c < 1 \mu\text{ms}^{-1}$  in camphor-doped samples.

### III. EXPERIMENTAL RESULTS

#### A. Growth facets of biphenyl crystals

In T-FG as well as T-DS, biphenyl crystals exhibited only two types of facets, namely, low-mobility {001} facets and high-mobility {110} facets. We give experimental evidence of the respective kinetics of these facets. Figure 3a shows a spatiotemporal (ST) diagram *-i.e.* a time series of binarized profiles of the growth front displayed in the reference frame of the sample- of a (001)-oriented biphenyl crystal during T-FG. The crystal first grows from a circular to a rhombus shape limited by {110} facets, then undergoes an impurity-driven (Mullins-Sekerka) instability, and finally settles into a steady dendritic regime with dendrites pointing in the  $\langle 100 \rangle$  and  $\langle 010 \rangle$  directions. The {110} facets are linked to each other by smooth rounded regions indicating that no forbidden orientation range exists in the non-faceted parts of the solid-liquid interface. The faceted parts of the profile remained rectilinear within the measurement uncertainty during the process. The measured angle between [110] and  $[1\bar{1}0]$  facets was of  $67.5 \pm 0.6^\circ$ . The small difference between this angle, and the one deduced from crystallographic data, if significant, is attributable to differences in temperature and composition. The slight crystallographic tilt of the {110} facets with respect to  $y$  was not resolved, but a difference in contrast between the faceted and rounded part of the interface was apparent, revealing a difference (planar versus rounded) in 3d shape between these two regions. The time evolution of the tip velocity  $V$  (Figure 3.b) shows that {110} facets developed through a perfectly smooth process indicating that no discontinuity in the kinetic coefficient is associated with {110} facets. The same features were also observed for {110} facets during T-DS, as will be

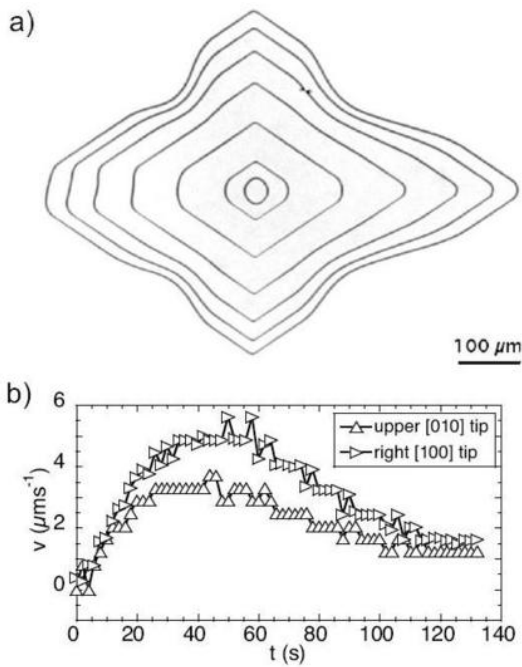


FIG. 3: a) ST diagram of a (001)-oriented biphenyl crystal during T-FG. Time interval: 20 s. A quench to  $\Delta T \approx 0.06$  K was applied to a quasi-circular seed at  $t = 0$ . b) Growth rates of the [100] (rightmost) and [010] (uppermost) tips as a function of time. The thermal time lag of the T-FG stage is about 1 min. The growth of the leftmost tip was perturbed by a dust particle.

seen in Section III C 1.

Detailed information about the growth kinetics of  $\{001\}$  facets was given by T-DS experiments performed without grain selection in as-quenched samples. Figure 4 shows a deep liquid pocket due to the mutual impingement of edge-on crystals adhering to the glass walls through their nonfaceted extremities. A sporadic nucleation of macrosk.jpg on the basal facets bordering the liquid pocket took place as  $\Delta T$  progressively increased until the whole pocket was suddenly filled by a polycrystal through an "explosive" nucleation process. The distance of the nucleation site from the growth front was of about 1.5mm corresponding to a temperature difference of about 9K.

In conclusion, the known absence of dislocations capable of serving as step sources for (001) facets –namely, dislocations with a [001] Burgers vector– in biphenyl crystals is a sufficient explanation of the low mobility of these facets. Reciprocally, the observed high mobility of  $\{110\}$  facets must be attributed to dislocations with [100] or [010] Burgers vector intersecting these facets. The only acceptable alternative would be the proximity of a roughening transition, but this seems very unlikely given the large extension of these facets, and the small growth rates considered in this study. However, the mechanisms by which  $\{110\}$  facets are fed with dislocations during growth even when the growth morphology becomes very

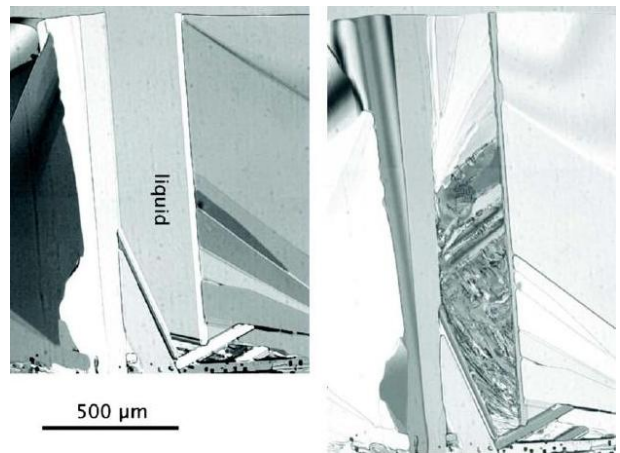


FIG. 4: T-DS of an as-quenched biphenyl sample consisting of many grains with different orientations at  $V = 6.5 \mu\text{ms}^{-1}$ . The growth direction is oriented upwards. Left: liquid pocket at the rear of the growth front. Right: same area (with differently oriented polars) after the pocket was solidified by explosive nucleation.

complex, are unknown. Anticipating on the observations presented below, we note that one, and probably the most important of these mechanisms is the plastic deformation generated by thermal stresses illustrated by GID. The formation of a stratified microstructure, or equivalently of (001) twist boundaries, during growth explained in Section III B 1 may also contribute, but it is not certain that these boundaries survive the morphological transitions of the system (see Fig. 13 below).

## B. Growth-induced plastic deformation during T-DS

### 1. GID in samples with single-crystal seeds

We performed T-DS experiments in a series of samples with single-crystal seeds with various in-plane orientations at values of  $V$  ranging from 0.5 to  $30 \mu\text{ms}^{-1}$ . In these samples,  $V_c \approx 15 \mu\text{ms}^{-1}$ , as previously mentioned. We observed GID processes with similar characteristics in all the experiments. This, and the fact that GID does not occur during T-FG, may suffice to establish that GID is not due to a cellular instability, but most probably to thermal stresses. However, to substantiate this conclusion, and because of the remarkable features of GID in our experiments, we study the geometry of this process in detail.

GID processes that took place in two different crystals oriented, one asymmetrically, and the other symmetrically, with respect to the T-DS setup are shown in Figures 5 and 6, respectively. Both processes go through the following three successive stages: Stage 1, which starts from the beginning of the solidification, and consists of the progressive amplification of a smooth contrast mod-

ulation extending along  $x$  (Fig. 7); Stage 2, which begins with the sudden creation of grain boundaries at positions corresponding to the extrema of the contrast modulation; Stage 3, during which crystal-glass collisions followed by the appearance of new grains lead to a fully polycrystalline microstructure.

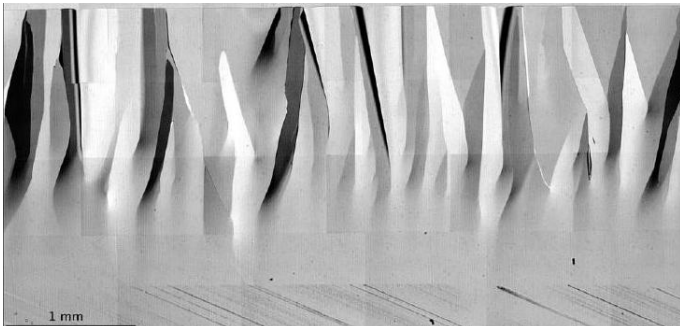


FIG. 5: GID during T-DS from a single-crystal seed with  $\theta_a = 24^\circ$ .  $V = 6.5 \mu\text{ms}^{-1}$ . The seed can be recognized from the [010] striation inherited from the post-T-FG cooling down of the sample.

Stage 1 clearly is a long-range process of plastic deformation of the growing crystal. A full understanding of such a process under the conditions of our experiments (strong confinement of the system and elastoplastic anisotropy of the solid) is notoriously beyond reach at present, but some interesting semi-quantitative remarks can be made. Various observations indicated that the distortion field existing in the crystal during Stage 1 mostly consisted of rotations of the crystal lattice about the [100] axis of the crystal. Such a distortion field favors the formation of tilt boundaries (arrays of [010] edge dislocations) in (010) planes, in agreement with the fact that the grain boundaries appearing at the onset of Stage 2 were approximately parallel to [100] in all the samples studied (Figs. 8 and 9). Figs. 6 and 7, on the one hand, and Fig. 10, on the other hand, correspond to two successive runs performed in the same (001)[100]-oriented sample at  $V = 30 \mu\text{ms}^{-1}$  and  $0.54 \mu\text{ms}^{-1}$ , respectively. The crystal length solidified during the first run was entirely re-melted before the second run so that there was no possible influence of the first GID on the second one. We note that  $V$  was above the cellular instability threshold during the first run, which is unimportant for our present purpose, but has interesting consequences, which will be commented later on. During these experiments, Stage 1 clearly exhibited two characteristic lengths, namely, a wavelength  $\Lambda_x$  along  $x$ , and a solidification length  $L_z$  along  $z$ . During both runs,  $\Lambda_x$ , defined as the spacing of the extrema of grey-level plots (Fig. 7), ranged from 300 to  $550 \mu\text{m}$ . This scatter was mostly due to the existence of a lateral gradient of unknown origin (but probably linked to some experimental imperfection). The value of  $L_z$ , defined as the solidification length between the start of the experiment and the first appearance of grain boundaries, was of  $500 \pm 50 \mu\text{m}$

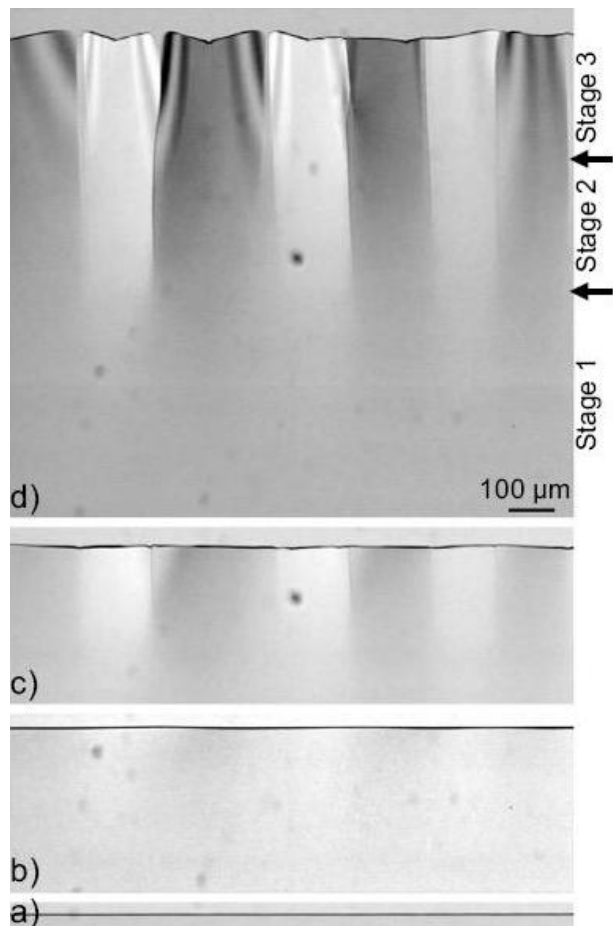


FIG. 6: GID during T-DS from a nearly (001)[100]-oriented single-crystal seed ( $\theta_a = -2.5^\circ$ ).  $V = 30 \mu\text{ms}^{-1}$ . **a**)  $t=0$  s (start of T-DS). **b**)  $t=22$  s. **c**)  $t=33$  s. **d**)  $t=46$  s. The two arrows indicate the appearance of grain boundaries and the first collisions with the glass plates, respectively.

in both experiments. Larger ranges of  $\Lambda_x$  and  $L_z$  were found in asymmetrically oriented crystals (Figs. 8 and 9) than in the (001)[100]-oriented ones, but the orders of magnitude remained the same. These observations indicate that  $\Lambda_x$  and  $L_z$  were essentially independent of  $V$ , as could be expected from the fact that the plastic deformation started from the beginning of the solidification. This suggests that these lengths are mostly determined by the geometry of the experiment.

Contrary to Stage 1, Stages 2 and 3 presented features, which depended on the in-plane orientation of the crystal, and on additional, ill-known, geometrical factors. This point is illustrated in Figs. 6 and 10, which show GID processes that occurred during two successive runs at different values of  $V$  in the same (001)[100]-oriented sample. The common features of the two runs are that the GID-induced microstructure kept the mirror symmetry about  $yz$  of the initial crystal as well as the periodicity inherited from Stage 1 (in contrast with what occurred in asymmetrically oriented samples), and that thickness fringes appeared near the grain boundaries at, or a short

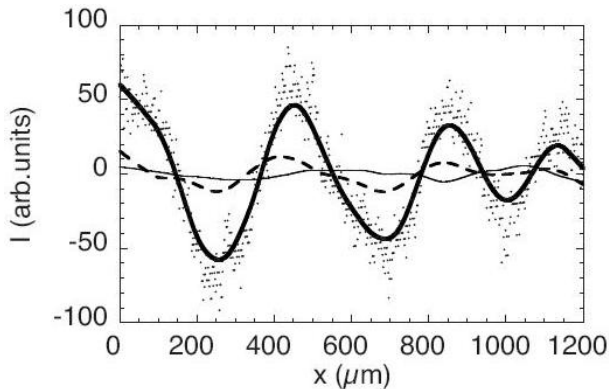


FIG. 7: Gray-level plots measured at different solidification length  $L_s$  during the T-DS run shown in Fig. 6. Thin line:  $L_s = 0$ . Broken line:  $L_s = 100\mu\text{m}$ . Thick line and dots:  $L_s = 200\mu\text{m}$ . The curves were obtained by smoothing the data points (dots) after subtraction of a linear function fitted onto the background.

time after, the onset of Stage 2. The most apparent differences between the two runs are the additional symmetry (twofold axis at  $\Lambda_x/4$ ) existing in Fig. 6 compared to Fig. 10, and the fact that the thickness fringes that appear on either side of a grain boundary are divergent in Fig. 6, but convergent in Fig. 10. Thickness fringes can only arise from ultra-thin crystal wedges. Figure 11 displays a schematic 3d reconstruction of the microstructures based on this remark, and the following additional conjectures: (i) the onset of Stage 2 occurred when the ongoing deformation made the crystal come into contact with the glass plates. At each point of contact, a pair of misoriented crystal wedges attached to the glass were created under the effect of external forces (linked with capillarity, flows in the liquid, changes in the thermal field); (ii) the initial positioning of the growing crystal with respect to the glass plates was symmetric in Fig. 6, but strongly asymmetric in Fig. 10. Regardless of the details, Fig. 11 illustrates the difference in nature between the early stages of GID, which do not involve contacts or collisions with the container walls, and later stages, which are essentially driven by such events. The specificity of GID, in the sense given to this term here, lies in Stage 1, while collision-induced deformations similar to those occurring during Stage 3 are also generated by a misaligned seed.

The nature of the growth process following crystal-glass collisions is most clearly illustrated in Figs. 10 and 8. Without discontinuity, and thus, probably through a plastic deformation of the crystal colliding the glass, solidification continues with the growth of (001)-oriented thin-film crystals in contact with, or very close to the glass walls. The extreme thinness of these crystals is revealed by a slight recoil of their solid-liquid interfaces with respect to thicker parts of the crystal attributable to their strong curvature in the direction  $y$  (Gibbs-Thomson effect).

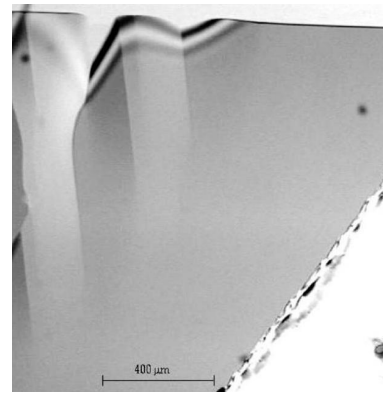


FIG. 8: GID during T-DS from an as-quenched seed with  $\theta_a = -6^\circ$ .  $V=1.55\mu\text{ms}^{-1}$ .  $\Lambda_x = 220\mu\text{m} \pm 20\mu\text{m}$ . The slanting edge of a grain selector appears in the lower-right hand corner of the photograph.

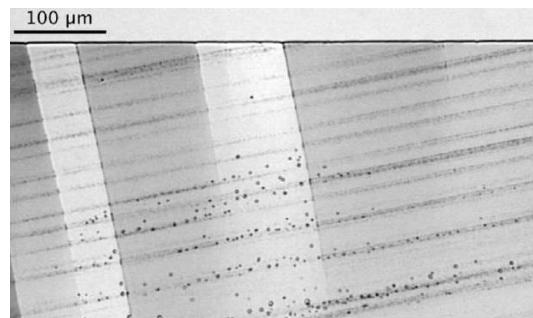


FIG. 9: GID during T-DS from a single-crystal seed with  $\theta_a = -10^\circ$ .  $V=0.3\mu\text{ms}^{-1}$ . After T-DS arrest, the heating of the ovens was switched off for a few hours, and then put on again. The grain boundaries are perpendicular to the [010] striation and thus parallel to [100].

## 2. Grain growth and GID in as-quenched samples

A spontaneous grain-growth process leading to a complete elimination of tilted grains in favor of (001)-oriented grains took place in as-quenched samples during the grain-selection stage of T-DS (Fig. 12). When their size permitted it, the (001)-oriented grains emerging from this process underwent a GID process similar to those observed in samples with single-crystal seeds. The GID process repeated itself with a constant amplification rate during the continuation of the growth through the funnel-shaped selector (Fig. 8). Adjacent (001)-oriented grains competed and often overlapped, leading to stratified microstructures (Fig. 13).

## 3. Cellular instability and GID

The rapid development of GID prevented us from observing deformation-free WF patterns in samples with single-crystal seeds. To bring about cellular transitions in deformation-free crystals, we applied upward  $V$ -jumps



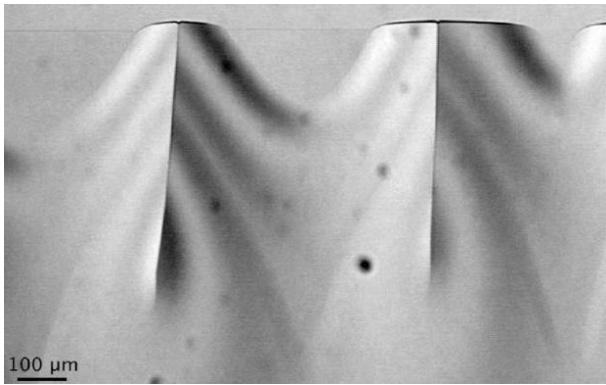


FIG. 10: GID during a second T-DS run in the same sample as in Fig. 6.  $V = 0.54 \mu\text{ms}^{-1}$ .  $\Lambda_x = 540\mu\text{m} \pm 20\mu\text{m}$ .

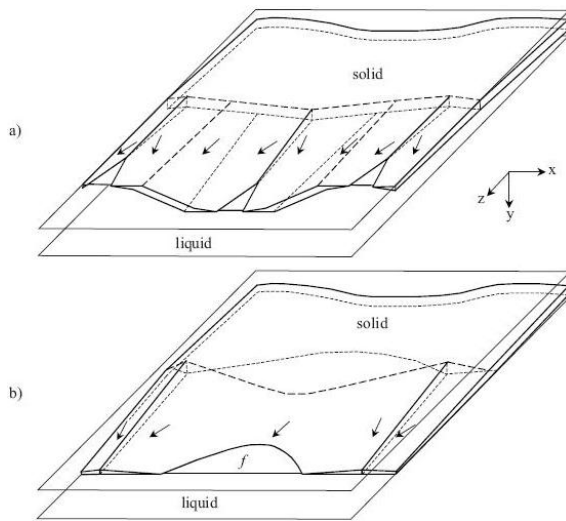


FIG. 11: Schematic 3D reconstruction of the crystal microstructures of Figs. 6 (a) and 10 (b).  $f$ : thin film crystal. Continuous lines: interfaces and grain boundaries. Broken lines: zones of rapid, but continuous change in orientation. Arrows: local orientations of the axis [100]. The sketches show a single period (along  $x$ ) of the GID microstructures.

to (001)-oriented grains at an early stage of GID in fresh undoped samples. Quite significantly, we never observed GID to appear after such a cellular transition occurred. In camphor-doped samples, cellular transitions without GID were observed at all the explored values of  $V$ .

Cellular-instability transients occurring concurrently with GID processes are worth briefly considering as a new instance of coupling between plastic deformation in the solid and impurity-driven dynamics at the growth front [33]. It is known that impurities rejected by the growing edge of a plate-like crystal partly segregate at the rear of this edge [34]. In the confined geometry of T-DS, this effect manifests itself by an increase of the equilibrium temperature, and thus an advance of the growth front, inversely related to the crystal thickness. Such a relation between the profile  $z = \zeta(x)$  of the growth front and the

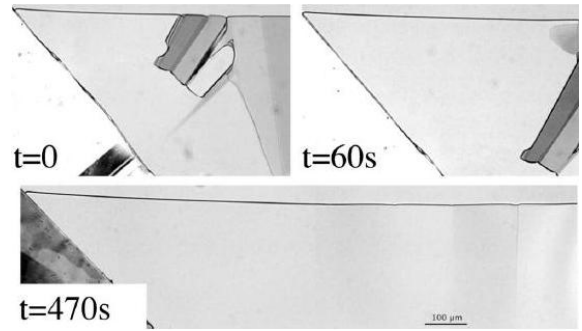


FIG. 12: Grain growth and onset of GID during the early stages of T-DS from an as-quenched seed.  $V = 3.1 \mu\text{ms}^{-1}$ . The slanting edge of a grain selector is visible in the lower-left hand corner of the photographs.

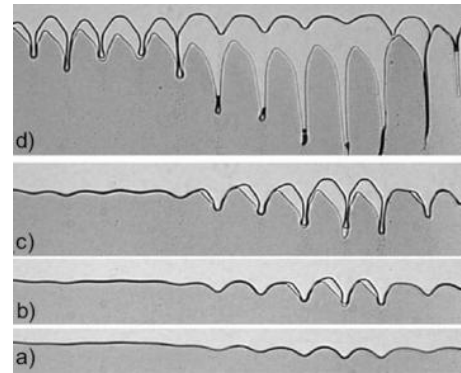


FIG. 13: Disclosure and elimination of a stratified microstructure during a cellular-instability transient.  $V = 4.7 \mu\text{ms}^{-1}$ . a)  $t = 0$ ; b)  $t = 34$  s; c)  $t = 40$  s and d)  $t = 56$  s. The difference in orientation of the stratums is about  $8^\circ$ . Horizontal dimension:  $620\mu\text{m}$ .

local value of the crystal thickness was observed during GID except in the thinnest regions of the front where the Gibbs-Thomson effect predominated. It should be noted that this impurity-driven effect, which remains small at low  $V$ , amplifies as  $V$  approaches  $V_c$  (Fig. 6) conferring an imperfect-bifurcation character to the cellular instability.

#### 4. Origin of GID

In conclusion, the core of the GID process is the progressive amplification of a long-range modulated plastic deformation of the growing crystals (Stage 1). The subsequent stages of the process are essentially geometrical consequences of this first stage. The lack of sensitivity of Stage 1 to the control parameters of the solidification rules out the possibility that this process be strongly connected with an impurity-driven dynamics. The fact, that in our system the growing crystals that underwent GID were not in contact with the container walls makes it very likely that the first stage of GID is basically due to

the thermal gradient alone –more precisely, the stresses engendered by an inhomogeneous temperature field in a crystal with strong elastic and plastic anisotropies. This stress field depends only on the geometry of the growing crystal at fixed geometry of the T-DS setup. This is consistent with the observed insensitivity of  $\Lambda_x$  and  $L_z$  to  $V$  and  $\theta_a$ , and suggests that the lack of GID in cellular fronts is simply due to the fact that stresses and plastic deformation are not transmitted from a cell to another.

### C. Weakly faceted cells and dendrites

#### 1. Stability of weakly faceted patterns

Like their non-faceted homologs, the WF patterns of biphenyl exhibited a broad ( $40 - 100\mu\text{m}$ , typically) range of stable spacings  $\lambda$  at fixed  $V$ . This range was bordered by a cell elimination instability at small  $\lambda$  and a cell splitting instability at large  $\lambda$ . We observed cell elimination processes during cellular-instability transients (Fig. 14), and could estimate the cell elimination threshold spacing to be about  $40\mu\text{m}$  in undoped biphenyl in the explored  $V$  range ( $V/V_c < 4$ ). On the other hand, we noted various modes of instability at  $\lambda > 100\mu\text{m}$ , in particular, oscillations and a propagating tip splitting (Fig. 15).

In their recent numerical study of the free growth of thin WF systems in a channel, Guérin *et al.* identified an oscillatory symmetry-broken mode of growth, and argued that this mode belongs to the same branch of states as the steady asymmetric fingers that exist in low-anisotropy nonfaceted systems [18]. In T-DS, such fingers, if any, should appear in the form of pairs of asymmetric fingers called *doublons* [8, 9, 35]. We performed a few experiments at very high  $V/V_c$  in camphor-doped biphenyl samples, and indeed observed a dendrite-to-*doublon* transition (Fig. 16) lending support to Guérin *et al.*'s argument. It must be noted, however, that we have not been able to ascertain the existence of facets at the tips of these *doublons*, so that the possibility of a roughening transition occurring in our system at high  $V$  cannot be entirely excluded.

#### 2. (001)[100]-oriented grains in undoped biphenyl

Cellular patterns were symmetric (*i.e.* did not drift in the direction  $x$ ) in (001)[100]-oriented grains of undoped biphenyl (Fig. 17), as could be expected since a mirror plane of the crystal structure is parallel to  $yz$  in these grains. The  $\lambda$ -distribution ranged from about  $40$  to  $100\mu\text{m}$  at the end of the cellular transition, and was slowly relaxing toward a uniform distribution. It was not possible to wait for this relaxation to be complete because the lifetime of the grains of interest was limited by the competition of the adjacent grains. We performed measurements in quiet regions of the evolving patterns assuming the quasi-steady-state condition

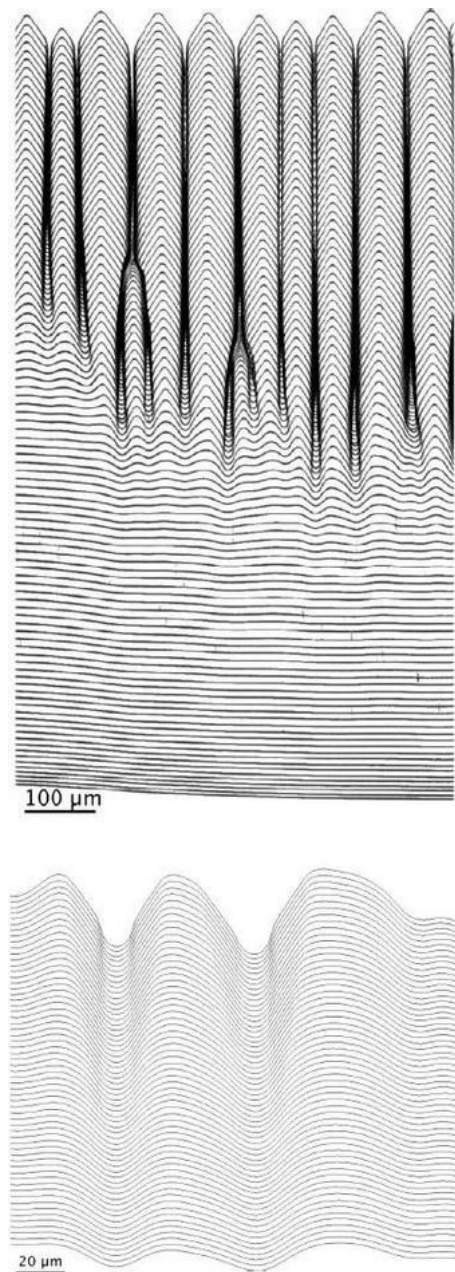


FIG. 14: ST diagram of a cellular-instability transient during T-DS of a (001)[100]-oriented grain. Time interval: 2 s (top), 0.08 s (bottom).  $V=6.5 \mu\text{ms}^{-1}$ .

to be valid in these regions. We measured the cell facet length and tip radius during three different T-DS runs in (001)[100]-oriented crystals of undoped biphenyl by the method explained in the legend to Figure 18. The results are displayed in Figure 19. The measurement error on  $l_f$  was of  $\pm 2\mu\text{m}$ , and thus of 10%, at worst, which can account for the scatter of the data. The major trend emerging from the data is an essentially linear increase of  $l_f$  with increasing  $\lambda$ . The concomitant increase in  $R$ , which is precursor to tip splitting, is much weaker. The dependence of  $l_f$  and  $R$  on  $V$  is undetectable. The frac-



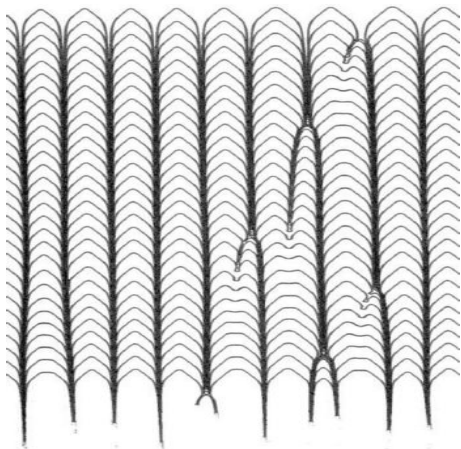


FIG. 15: ST diagram (time intervals 2 s) of a propagating tip-splitting instability during T-DS of a (001)[100]-oriented grain.  $V=17 \mu\text{ms}^{-1}$ . Note the transient oscillations in the wake of the solitary wave. Horizontal dimension:  $620 \mu\text{m}$ . The diagram has been contracted by a factor of 2 vertically.

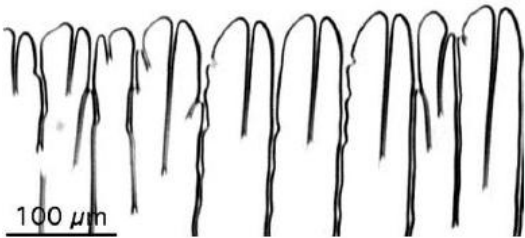


FIG. 16: *Doublons* during T-DS of a (001)-oriented grain. Camphor-doped biphenyl.  $V=150 \mu\text{ms}^{-1}$ .

tion of the front occupied by facets ( $\approx 0.5$ ) is important, and increases as  $\lambda$  increases. The sidebranching threshold is thus shifted to high values of  $\lambda$  compared to what it would be without facets. This effect is most clearly illustrated by the long distance separating the first sidebranches from the tips of tilted dendrites in Figure 24 below.

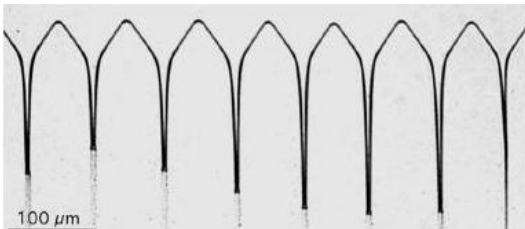


FIG. 17: Cellular pattern during T-DS of a [001](100)-oriented crystals. Undoped biphenyl.  $\theta_a \approx 1^\circ$ .  $V = 6.5 \mu\text{ms}^{-1}$ .

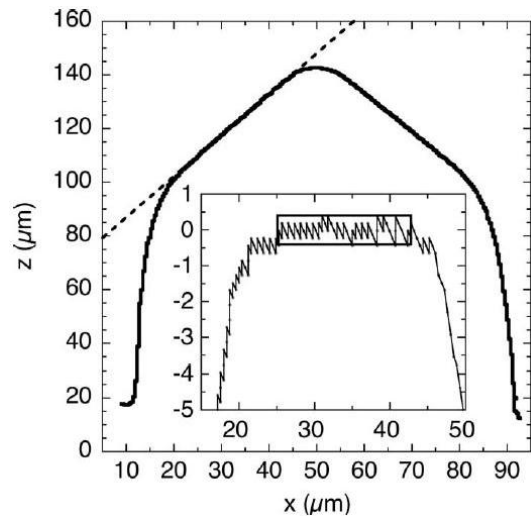


FIG. 18: Determination of the length and orientation of a facet in a T-DS cell. The profile was extracted from Fig. 17a by thresholding and skeletonizing the image of a cell. The broken line is the linear best-fit function along a presumed facet. This function was subtracted from the relevant part of the profile yielding the set of data points displayed in the inset. The box encloses the data points whose deviation from a smooth curve drawn through these points is smaller than their scatter. The length of the box (corrected for the projection factor) was taken as a measure of the facet length.

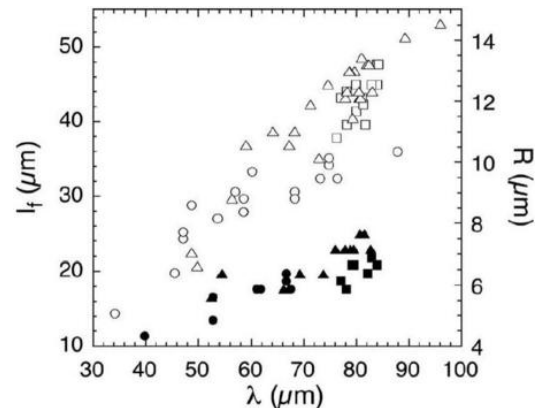


FIG. 19: Facet length  $l_f$  (open symbols) and tip radius  $R$  (filled symbols) versus cell spacing  $\lambda$  during T-DS of (001)[100]-oriented crystals. Undoped biphenyl. Squares:  $V = 4.7 \mu\text{ms}^{-1}$ . Triangles:  $V = 6.2 \mu\text{ms}^{-1}$ . Disks:  $V = 17 \mu\text{ms}^{-1}$ .

### 3. WF cellular patterns as a function of in-plane orientation in camphor-doped biphenyl

The grain-growth process studied in Section IIIB 2 yielded (001)-oriented grains with in-plane orientations belonging to a limited interval around  $\theta_a = 0$ . We used a rotating T-DS stage to grow (001)-oriented crystals with arbitrary  $\theta_a$  values in camphor-doped biphenyl samples. The uncertainty on  $\theta_a$  was of  $\pm 0.2^\circ$ . At all  $\theta_a$  values

cell tips exhibited well-defined facets, which were however too small to permit a quantitative study. We observed a lateral drift of the cellular patterns for all the in-plane orientation of the crystal except the (001)[100]- and (001)[010]-orientations (Fig. 20 and 21). In the last-named orientation, the crystal structure is not invariant to reflection with respect to the  $yz$  plane, but the absence of drift indicates that the whole system has such an invariance. (It should be noted that monoclinic angle of biphenyl is small). In other words, the behavior of the system was practically that of a 2D system with two orthogonal symmetry axis ([100] and [010]). It is worth noting that, contrary to [100] cells, [010] cells did not exhibit tip splitting but transformed to dendrites at large spacing values (Fig. 22).

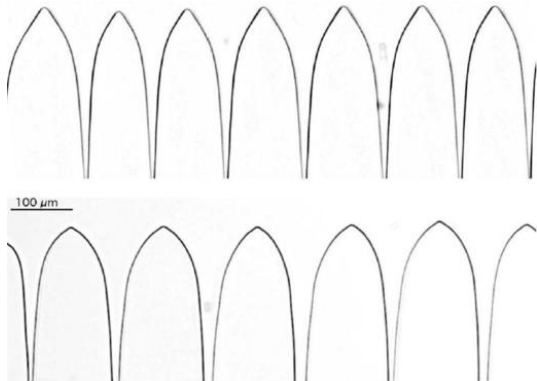


FIG. 20: Cellular patterns during T-DS in camphor-doped biphenyl. Above: (001)[100]-oriented crystal.  $V = 10.0 \mu\text{ms}^{-1}$ ; below: (001)[010]-oriented crystal.  $V = 5.0 \mu\text{ms}^{-1}$ .

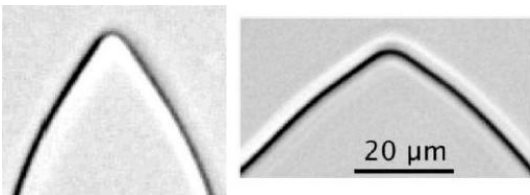


FIG. 21: Enlargement of cell tips from Fig. 20. Left: [100] cell. Right: [010] cell.

We studied the lateral drift of the cellular patterns in grains with  $\theta_a \neq 0$  and  $\theta_a \neq \pi/2$ . Like in nonfaceted systems [10, 36], the tilt angle of the direction of growth of the cell tips was an increasing function of  $V$  and approached the tilt angle of the nearest axis of symmetry of the system ( $\theta_a$  or  $\pi/2 - \theta_a$ ) at large values of  $V/V_c$  (Fig. 22).

Figure 23 shows the ST diagram of a cellular-instability transient in a crystal with  $\theta_a = 40 \pm 1^\circ$ . Though the shape of the cells rapidly departed from a mere sine, no drift of the structure was observed until facets appeared. Given that kinetic anisotropy controls the drift velocity during the first stages of the cellular transient [37], this indicates

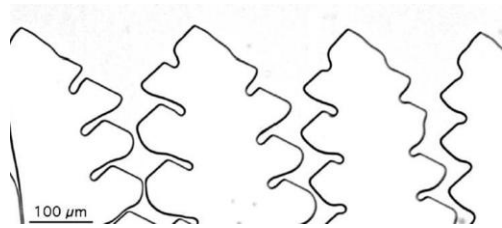


FIG. 22: [010] dendrites during T-DS of a (001)-oriented grain with  $\theta_a = 82^\circ$ . Camphor-doped biphenyl.  $V = 10 \mu\text{ms}^{-1}$ . The tilt angle of the dendrites is  $8 \pm 1^\circ$ .

that this anisotropy is relatively weak for  $\mathbf{n}$  belonging to the basal plane of biphenyl. Finally, we note that grains with a {110} facet nearly perpendicular to the growth axis exhibited a singular dynamics displaying a coexistence between crenellated interfaces [19, 20, 24], [100]-dendrites and [010]-dendrites during cellular-instability transients (Fig. 24).

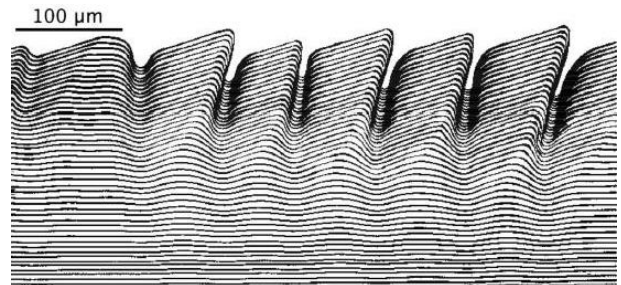


FIG. 23: ST diagram (length of sequence 48s) of a cellular-instability transient during T-DS of a (001)-oriented grain with  $\theta_a = 40 \pm 1^\circ$ . Undoped biphenyl.  $V = 6.2 \mu\text{ms}^{-1}$ .

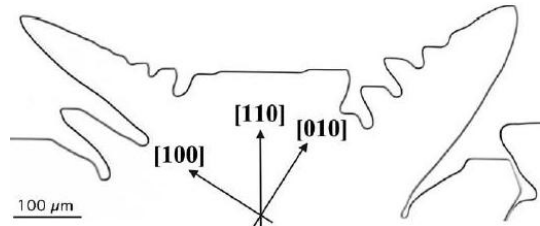


FIG. 24: Cellular-instability transient during T-DS of a (001)-oriented grain with a {110} facet nearly perpendicular to  $z$ . Camphor-doped biphenyl.  $V = 10 \mu\text{ms}^{-1}$ . The angle of the facet to  $z$  is about  $88.5^\circ$ .

#### IV. CONCLUSION

A thin plate-like crystal confined between two walls and submitted to directional solidification is prone to plastic deformation under the effect of thermal stresses generated by the applied thermal gradient, and interactions with the walls. This study has shown that

a deformation-free directional solidification of plate-like crystals is feasible, at least in the case of impure systems, and provides a good experimental model of the dynamics of 2D weakly faceted directional solidification. We have presented first elements of an experimental investigation of this dynamics, including a set of preliminary quantitative data about the facet lengths of steady WF cellular patterns as a function of  $\lambda$  and  $V$ . Previous experimental and theoretical studies have established that the scaling laws of nonfaceted dendritic free growth still hold in weakly faceted systems. Similarly, although in a less precise way, this study has shown that the dynamics of weakly faceted directional-solidification systems is similar to that of anisotropic, but nonfaceted systems, except, perhaps, when the growth front is nearly parallel to a facet. Theoretical studies pointed out that the length of the facets near dendrite tips, which is directly

connected to the capillary and kinetic coefficients of the solid-liquid interface, is the most specific feature of WF growth morphologies. Further experimental and numerical studies of the facet lengths of steady WF cellular patterns as a function of various control, and material parameters could cast light upon basic questions such as the respective roles of capillary and kinetic anisotropies in weakly faceted growth.

### Acknowledgments

T.B. acknowledges support by the European Community (Contract No. HPMF-CT-1999-00132) and by the Hungarian Scientific Research Fund (Contract No. OTKA-K-62588).

- 
- [1] M. Asta, C. Beckermann, A. Karma, W. Kurz, R. Napolitano, M. Plapp, G. Purdy, M. Rappaz, R. Trivedi, *Acta Mater.* **57**, 941 (2009). See also W.J. Boettinger, S.R. Coriell, A.L. Greer, A. Karma, W. Kurz, M. Rappaz, R. Trivedi, *Acta Mater.* **48**, 43 (2000).
  - [2] J.W. Rutter and B. Chalmers, *Can. J. Phys.* **31**, 15 (1953).
  - [3] W.W. Mullins and R.F. Sekerka: *J. Appl. Phys.* **35**, 444 (1964).
  - [4] P. Kurowski, C. Guthmann and S. de Cheveigné, *Phys. Rev. A* **42**, 7368 (1990).
  - [5] M. Ben Amar and Y. Pomeau, *Europhys. Lett.* **2**, 307 (1986).
  - [6] A. Barbieri, D.C. Hong and J.S. Langer: *Phys. Rev. A* **35**, 1802 (1987).
  - [7] E. A. Brener, H. Müller-Krumbhaar and D.E. Temkin, *Europhys. Lett.* **17**, 535 (1992).
  - [8] T. Ihle and H. Müller-Krumbhaar, *Phys. Rev. E* **49**, 2972 (1994).
  - [9] S. Akamatsu, G. Faivre and T. Ihle, *Phys. Rev. E* **51**, 4751 (1995).
  - [10] S. Akamatsu and T. Ihle, *Phys. Rev. E* **56**, 4479-4485 (1997).
  - [11] W.K. Burton, N. Cabrera and F.C. Frank: *Phil. Trans. Soc. London* **243A**, 299 (1951).
  - [12] A.A. Chernov, *Contemporary Phys.*, **30**, 251 (1989).
  - [13] J. Maurer, P. Bouissou, B. Perrin and P. Tabeling, *Europhysics Letters* **8**, 67 (1989).
  - [14] M. Ben Amar and Y. Pomeau, *Europhys. Lett.* **6**, 609 (1988).
  - [15] M. Adda Bedia and V. Hakim, *J. Phys. I* **4**, 383 (1994).
  - [16] M. Adda Bedia and M. Ben Amar, *Phys. Rev. E* **51**, 1268 (1995).
  - [17] J.-M. Debierre, A. Karma, F. Celestini and R. Guérin, *Phys. Rev. E* **68**, 041604 (2003).
  - [18] R. Guérin, J.-M. Debierre, K. Kassner, *Phys. Rev. E* **71**, 011603 (2005).
  - [19] R. Bowley, B. Caroli, C. Caroli, F. Graner P. Nozières and B. Roulet, *J. Phys. (Paris)*, **50**, 1377 (1989).
  - [20] B. Caroli, C. Caroli and B. Roulet, *J. Phys. (Paris)*, **50**, 3075 (1989).
  - [21] M. Adda Bedia and M. Ben Amar, *Phys. Rev. A* **43**, 5702 (1991).
  - [22] T. Uehara, R.F. Sekerka, *Journal of Crystal Growth* **254**, 251 (2003).
  - [23] T. Börzsönyi, S. Akamatsu and G. Faivre, *Lecture Notes in Computational Science and Engineering* **32**, 166 (2003).
  - [24] F. Melo and P. Oswald, *Phys. Rev. Lett.*, **64**, 1381 (1990).
  - [25] T. Börzsönyi, S. Akamatsu and G. Faivre, *Phys. Rev. E* **65**, 011702 (2001).
  - [26] T. Börzsönyi and S. Akamatsu, *Phys. Rev. E* **66**, 051709 (2002).
  - [27] L.M. Fabietti, R. Trivedi, *J. Crystal Growth* **173**, 503 (1997).
  - [28] J. Trotter, *Acta Cryst.*, **14**, 1135 (1961).
  - [29] A. Hargreaves and S.H. Rizvi, *Acta Cryst.* **15**, 365 (1962).
  - [30] R.K. Marwaha and B.S. Shah, *Cryst. Rech. Technol.* **27**, 1097 (1992).
  - [31] J. Mergy, G. Faivre, C. Guthmann and R. Mellet, *J. Cryst. Growth* **134**, 353 (1993).
  - [32] S. Akamatsu and G. Faivre, *J. Phys. I* **6**, 503 (1996).
  - [33] S. Bottin-Rousseau, S. Akamatsu, and G. Faivre, *Phys. Rev. B* **66**, 054102 (2002).
  - [34] T. Fujioka and R.F. Sekerka, *J. Cryst. Growth* **24/25**, 84 (1974).
  - [35] B. Utter, R. Ragnarsson and E. Bodenschatz, *Phys. Rev. Lett.* **86**, 4604 (2001).
  - [36] J. Deschamps, Thèse de Doctorat, Université Aix-Marseille I, 2007.
  - [37] S.R. Coriell and R.F. Sekerka, *J. Cryst. Growth* **34**, 157 (1976).